

Article

Effect of the Cooling Rate of Thermal Simulation on the Microstructure and Mechanical Properties of Low-Carbon Bainite Steel by Laser-Arc Hybrid Welding

Jintao Chen ¹, Zhenlin Zhang ¹, Zhiyi Zhang ^{1,2}, Yingzong Liu ¹, Xu Zhao ³, Jingqing Chen ^{1,*} and Hui Chen ^{1,*}

¹ Key Laboratory of Advanced Technologies of Materials, Ministry of Education, School of Materials Science and Engineering, Southwest Jiaotong University, Chengdu 610031, China; cjt@my.swjtu.edu.cn (J.C.); zzl21@swjtu.edu.cn (Z.Z.); zhangzhiyi@cqsf.com (Z.Z.); yingzongliu123@163.com (Y.L.)

² CRRC Qingdao Sifang Co., Ltd., Qingdao 261111, China

³ State Key Laboratory of Traction Power, Southwest Jiaotong University, Chengdu 610031, China; zhaoxu145833@163.com

* Correspondence: simweld@163.com (J.C.); xnrpt@swjtu.edu.cn (H.C.)

Abstract: A new kind of low-carbon bainite steel with excellent strength and toughness was developed, serving as the bogie of the next-generation high-speed train. However, the softening of the heat-affected zone (HAZ) in laser-arc hybrid welding (LAHW) needs to be overcome. In this study, the effect of the cooling rate of the LAHW process on the microstructure and mechanical properties in the HAZ was explored via thermal simulation. The results showed that with increased cooling rate, the grain size increased, the content of lath martensite decreased, and the lath bainite gradually changed to a granular shape in the thermal simulation specimen. With the decrease in the cooling rate, i.e., with the increase of $t_{8/5}$, the strength–toughness matching of the material showed a downward trend. The thermal simulation specimen with a $t_{8/5}$ of 6–8 s had higher strength and good toughness, which can be considered a potential welding parameter reference. The content of martensitic austenite (M-A) constituents was the main factor that determined the strength and toughness of the joint. During the tensile test, the axial force caused the material to tighten, and the transverse stress as obvious in the part of the M-A constituents that are prone to microcracks and many defects, resulting in cracks, paths, and multi-component layers in the center. As a result, the thermal cycle specimens had mixed fracture characteristics.

Keywords: thermal cycle simulation; low-carbon bainite steel; microstructure; M-A constituents; cooling rate



Citation: Chen, J.; Zhang, Z.; Zhang, Z.; Liu, Y.; Zhao, X.; Chen, J.; Chen, H. Effect of the Cooling Rate of Thermal Simulation on the Microstructure and Mechanical Properties of Low-Carbon Bainite Steel by Laser-Arc Hybrid Welding. *Coatings* **2022**, *12*, 1045. <https://doi.org/10.3390/coatings12081045>

Academic Editor: Rafael Comesaña

Received: 27 June 2022

Accepted: 19 July 2022

Published: 24 July 2022

Publisher's Note: MDPI stays neutral with regard to jurisdictional claims in published maps and institutional affiliations.



Copyright: © 2022 by the authors. Licensee MDPI, Basel, Switzerland. This article is an open access article distributed under the terms and conditions of the Creative Commons Attribution (CC BY) license (<https://creativecommons.org/licenses/by/4.0/>).

1. Introduction

Lightweight bogie materials are among the effective ways to reduce the weight of next-generation high-speed trains and to upgrade their performance. The new generation of low-carbon bainite steel obtained by the thermo–mechanical controlled cold rolling process has been widely used in the shipbuilding, construction, and transportation fields due to its excellent strength and toughness, and its performance also meets most of the service requirements of high-speed railway bogies. Therefore, the method of increasing the strength level of bogie steel and reducing the plate thickness could effectively achieve the goal of lightweight bogie materials [1]. The manufacturing process of structural parts is inseparable from welding technology. Currently, gas-shielded metal arc welding (GMAW) and submerged arc welding (SAW) are mostly used for high-strength and low-carbon bainitic steel; nevertheless, these methods have disadvantages such as a large heat input, large deformation after welding, and low efficiency [2–4]. Laser-arc hybrid welding (LAHW) has the characteristics of a good bridging ability, small heat-affected zone (HAZ), and high efficiency due to the addition of a laser with good penetration and concentrated

energy [5], which has become one of the ideal technologies to achieve high-quality welding of key components of high-speed railway car bodies and bogies [6]. However, in the LAHW process of low-carbon bainite steel, the welded joint of the base material (BM) cannot achieve the original mechanical properties attributed to the welding thermal cycle of the heating speed, which is responsible for the characteristics of the local uneven cooling speed. As a result, the HAZ in the joint turns into the main weak area, especially the coarse-grained heat-affected zone (CGHAZ), limiting its application [7,8].

The welding thermal cycle describes the heating and cooling processes of a certain point in the welded joint, which is a comprehensive reflection of the welding heat input and welding process. Its main parameters include the heating rate, peak temperature, cooling rate, and residence time above the phase transition temperature. Zhang et al. [9] showed that the peak temperature of the welding thermal cycle had a great influence on the volume fraction and size of the hardened precipitated phase in aluminum alloy. However, for steel, due to the short heating stage and wide heating range of the welding thermal cycle, the weld center temperature usually exceeds 1350 °C, resulting in the rapid growth of weld grain and an increase in the HAZ. Austenite transformation occurs in the cooling process, which can easily result in coarse grain with a transformed structure, so it is critical to control the cooling rate of the joint [10]; “ $t_{8/5}$ ”, referring to the cooling time from 800 to 500 °C, is usually adopted as an indicator of the cooling rate. Zavdoveev et al. [11] showed that the welding thermal cycle cooling rate of ferritic pearlite steel was 10–15 °C/s to obtain mechanical properties similar to that of the BM, while the cooling rate of bainitic steel was 10–25 °C/s. Lan et al. [12] revealed that when the cooling time of low-carbon multi-micro alloy steel ranged from 30 to 120 s, the final microstructure morphology gradually changed from bainite ferrite to granular bainite.

The types and morphologies of the microstructure can affect the mechanical properties of materials. Studies [13,14] showed that the size of grain in CGHAZ and martensitic austenite (M-A) constituents in the joint were vital factors affecting the toughness. Generally, the M-A constituents can seriously reduce the toughness of the HAZ. Chen et al. [13] reported that the microscopic mechanism of cleavage cracking in specimens with a simulated HAZ was controlled by the size of the M-A constituents. The larger the size of the M-A constituents, the smaller the critical loads of crack nucleation. For cleavage crack propagation, microstructure characteristics such as dislocation structure, grain boundary disorientation, and amount of ferrite in the grain have a decisive influence on the cleavage crack propagation ability [14,15]. Davis et al. [16] found that the M-A constituents were the hard-brittle phase prone to cracking, and the stress concentration phenomenon could occur in the ferrite matrix near M-A constituents, increasing the cracking tendency. Di et al. [17] found that the M-A constituents with a necklace structure had poor toughness at a lower second peak temperature in multi-layer multi-pass welding. The volume fraction and size of M-A have a great influence on the toughness degradation. Huda et al. [18] found that different cooling rates lead to changes in the size, distribution, and morphology of the M-A constituents. Compared with a cooling rate of 2 °C/s, a cooling rate of 10 °C/s showed higher tensile strength and ductility. Cui et al. [8] found that a brittle zone appeared in the subcritical reheat CGHAZ in the HAZ of welding through the thermo-mechanical simulator, in which a large amount of residual austenite and cementite precipitation significantly reduced the impact toughness, while the supercritical reheat CGHAZ had the highest impact toughness, and the fracture mode was a mainly ductile fracture, with dimples formed by the micropore polycondensation mechanism. It can be concluded that the fracture properties of low-carbon bainite steel welded joints depend on the coarse-grained microstructure and composition of the HAZ, while the microstructure and properties of coarse grain can be controlled by changing the cooling rate of the welding thermal cycle. Since the CGHAZ has poor performance, the influence of the post-welding cooling speed on the microstructure and mechanical properties of the joint has still not been detailed due to the short heating time, concentrated heat source, and relatively high cooling speed of LAHW.

Therefore, thermal physics experiments were used to simulate the LAHW process under different cooling rates, and the microstructure evolution dynamics of the coarse grain zone of the joint in the HAZ was obtained in this study. Furthermore, the effect of the microstructure formed at specific cooling rates in the coarse-grained zone on the tensile properties and fracture was studied. Finally, the mechanism of the M-A constituents in the cooling process was analyzed. The interpretation could further provide technological guidance for high-strength and low-carbon bainite steel of LAHW.

2. Material and Experimental Procedure

2.1. Material

The BM used in this study is a kind of high-strength low-carbon bainitic steel (ASTM A1066/A1066M); the hot-rolled state and the ER80YM filler wire with a diameter of 1.2 mm were used. Their chemical compositions are given in Table 1, and the micro-morphology of the BM is shown in Figure 1. The microstructure and grains are small, with a size of about 5–20 μm , mainly lath bainite (LB), granular bainite (GB), and ferrite (F), of which the LB is intermittently distributed in Figure 1. The basic mechanical properties of the BM are shown in Table 2.

Table 1. Main alloying elements of the BM and ER80YM filler wire (wt.%).

Materials	C	Mn	Si	S	P	Al	Nb	Mo	Ti	V	Fe
BM	0.081	1.86	0.06	0.0025	0.010	0.029	0.051	0.20	0.08	0.003	Bal.
ER80YM	0.057	1.49	0.37	0.005	0.008	0.34	2.84	0.35	-	-	Bal.

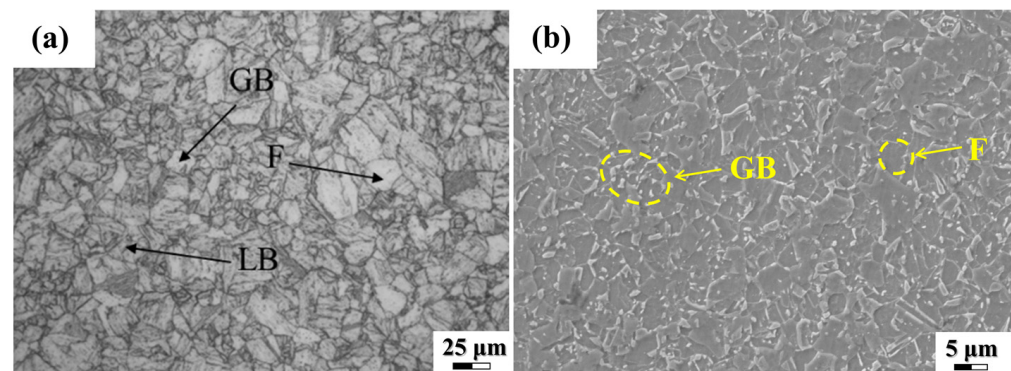


Figure 1. The microstructure of the BM: (a) optical microscope (OM) (b) scanning electron microscope (SEM).

Table 2. Basic mechanical properties of the BM.

Tensile Strength R_m /MPa	Yield Strength $R_{p0.2}$ /MPa	Elongation/%	$-40\text{ }^\circ\text{C}$ AKv/J
811	732	25.4	50

2.2. Thermal Simulation Experiment

" $t_{8/5}$ " is usually adopted as an indicator of the cooling rate, representing the cooling time from 800 to 500 $^\circ\text{C}$, which can not only reflect the cooling speed but also directly reflects the thermal cycle process of different types of steel. Therefore, this paper compares different cooling rates through different $t_{8/5}$ values. To ensure the reliability of the welding thermal simulation experiment, thermocouple temperature measurement is used to verify the thermal cycle parameters of each micro-zone in the HAZ during the actual welding process.

Before carrying out the thermal simulation experiment, a disk laser TRUMPF LASER TruDisk 10002 (Ditzingen, Germany) and electric welding machine Fronius TransPuls Synergic 4000 (Wels, Austria) were used to complete plate butt welding to obtain the actual thermal cycle parameters. A single weld bead was acquired since the efficiency of LAHW is high for 6-mm-thick plate welding. The welding process parameters are shown in Figure 2,

with defocusing quantity 0, light wire spacing 2 mm, and I-type groove and butt clearance 1.2 mm. The laser power was 4800 W, with a wire feeding speed of 13 m/min and a welding speed of 26 mm/s, using a mixture of 80% Ar + 20% CO₂ and protected airflow of 25 L/min. As shown in Figure 2b, the thermal cycle parameters of each micro-zone in the HAZ during the welding process are collected by the thermocouple temperature measurement test method. There are three temperature measuring points, which are point A, B, and C, with 10 mm between the temperature measuring points and 4.8, 5.2, and 5.5 mm from the weld center. A spot welder was used to fix the K-type thermocouple on the surface of the weldment. At the beginning of the actual welding process, the thermal cycle acquisition command was triggered to obtain the temperature change history of the collection point. As shown in Table 3, points A and B are the corresponding test points near the CGHAZ, and their cooling rate was about 25~35 °C/s; the corresponding $t_{8/5}$ ranged from 8~12 s.

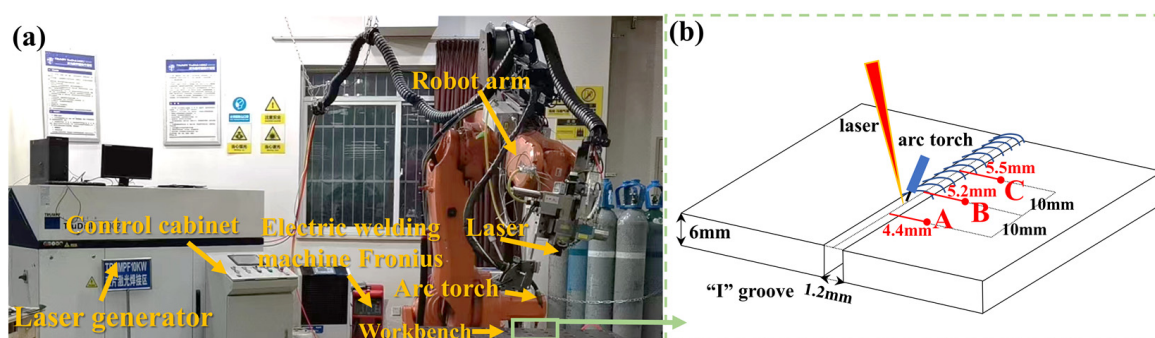


Figure 2. (a) Welding system, (b) Schematic diagram of the thermal cycle sampling point for the plate butt welding.

Table 3. The thermal cycle in A, B, and C (single weld bead only).

Location	Peak Temperature (°C)	Cooling Rate (°C/s)	$t_{8/5}$ (s)
A	1210 ± 50.5	~29.41	10.2
B	990 ± 42.3	~25.64	11.7
C	890 ± 52.4	~24.39	12.3

The Gleeble-540 thermo–mechanical machine (Poestenkill, NY, USA) was used to simulate the thermal cycle in the microzone of the weld HAZ. According to the actual welding process results, the Rykalin-2D program, which is similar to the laser-arc hybrid heat source with a heating rate of about 416 °C/s, was selected to control the peak temperatures of 750, 850, 950, 1050, 1150, and 1250 °C. The peak temperature retention time was set to 0.01 s, and $t_{8/5}$ was adjusted. Thermal cycle curves under each parameter were recorded, and 3 parallel specimens were set for each group of parameters. Figure 3 shows the thermal cycle curve under different cooling speeds and $t_{8/5}$ parameter settings. The specimens were heated at the same speed, and the corresponding cooling speed ranged from 16.5 to 75 °C/s. The above tests were completed in four groups, of which one group was sampled for microstructure analysis and the rest for mechanical properties.

2.3. Microstructure Analysis Test

The specimen of the simulated HAZ thermal cycle was cut transversely along the heating part of the specimen center by wire cutting, and the specimen size was $\Phi 6 \text{ mm} \times 5 \text{ mm}$. Then, the metallographic specimens are ground, polished, and etched with NITAL 4%. The microstructure of the BM, the thermal cycle specimen sections, and the tensile fracture were observed and analyzed by a Zeiss A1M optical microscope (Oberkochen, Germany) and field emission scanning electron microscope (FE-SEM, JSM-7800F, JEOL, Tokyo, Japan). The grain size was measured by the cross-point method under an optical microscope according to the GB/T 6394 standard [19].

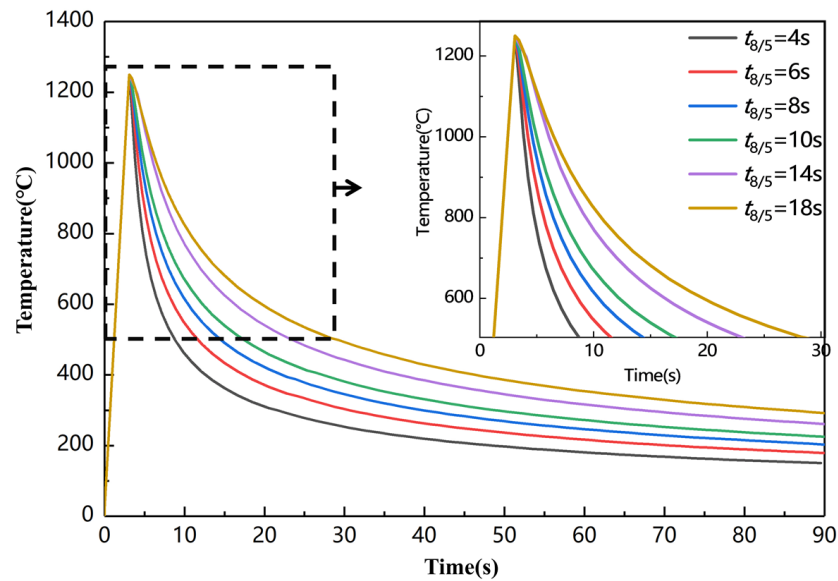


Figure 3. Test thermal cycle curves at different $t_{8/5}$ values of $T_{\max} = 1250$ °C.

2.4. Mechanical Property Test

The HVS-300 Vickers hardness tester (Mineola, NY, USA) was used to examine the hardness of the thermal simulation specimens with different parameters. The holding time was 15 s, and the loading force was 1 kg. Five points were randomly selected from each section to test. Then, the tensile test was carried out on a DNP-300 universal testing machine (Tokyo, Japan). As shown in Figure 4, the thermal simulation specimens were processed into tensile specimens, whose working section length was 18 mm, and the tensile properties of the thermal simulation specimens were tested. The tensile test was carried out at room temperature (20 °C) with a tensile rate of 2 mm/min to obtain the tensile strength of each thermal simulated specimen.

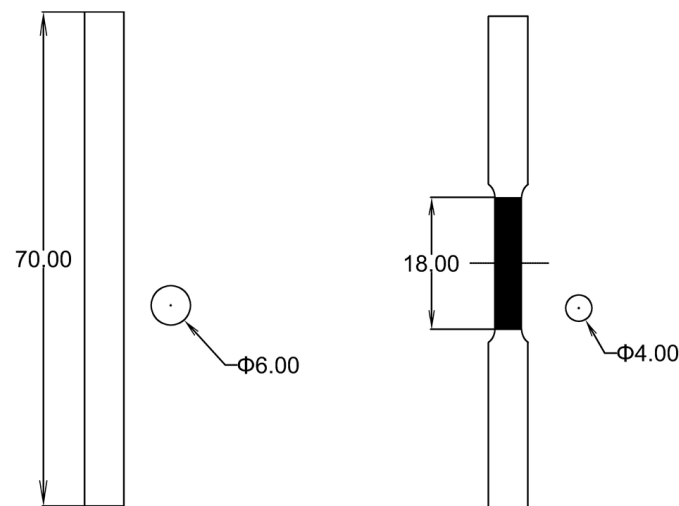


Figure 4. Specimen used for thermal simulation in the tensile test ($\Phi = 4$ and 6 mm in the picture).

3. Results

3.1. Microstructure of the Thermal Simulation Specimen

As shown in Figure 5, the microstructure morphology of the CGHAZ under different cooling times at a peak temperature of 1250 °C was obtained by welding thermal cycle simulation. As can be seen from Figure 5a, the HAZ was mainly composed of bainite with different contents of low-carbon lath martensite (LM) and ferrite. After thermal cycling,

the grain size of the metal was about 10–20 μm ($t_{8/5} = 4$ s). When $t_{8/5}$ was in the range of 4 to 18 s, the grain size increased gradually with the decrease of the cooling rate, and the boundary of the grain became blurred, which mainly accounted for more time for phase transformation during the slower cooling rate. Carbon atoms were more fully dispersed at the grain boundary in the process of grain growth, thus avoiding the generation of more hardened martensite and gradually generating the mixed structure of martensite and ferrite [20].

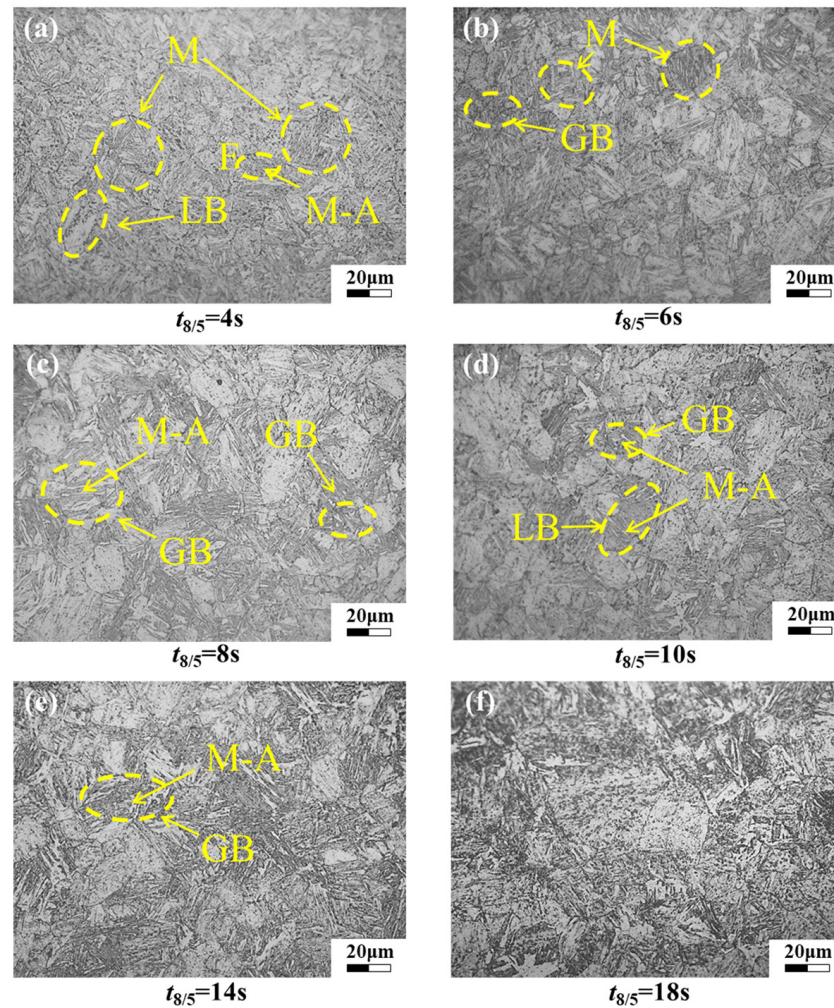


Figure 5. Different $t_{8/5}$ thermal simulations of the HAZ microstructure (OM) when $T_{\text{max}} = 1250$ °C. (a) $t_{8/5} = 4$ s; (b) $t_{8/5} = 6$ s; (c) $t_{8/5} = 8$ s; (d) $t_{8/5} = 10$ s; (e) $t_{8/5} = 14$ s; (f) $t_{8/5} = 18$ s.

When the cooling rate was fast, namely, $t_{8/5} = 4$ and 6 s, shown in Figure 5a,b, the microstructure of the CGHAZ in the thermal cycle was mainly LM, and a small amount of LB, GB, and F. The M-A constituent was granular around F, but smaller in size. When $t_{8/5} = 8$ and 10 s, i.e., a slower cooling rate, shown in Figure 5c,d, the content of M gradually decreased, and elongated M-A constituents began to appear. The CGHAZ was gradually dominated by LB and GB. When the austenitizing transformation was complete, as the cooling rate continued to decrease, shown in Figure 5e ($t_{8/5} = 14$ s) and Figure 5f ($t_{8/5} = 18$ s), the grain size increased significantly with an average size of about 30 μm . In Figure 5e, LM was reduced, and most of the microstructure was LB and a small amount of GB. GB contained a mixed-phase structure of M-A constituents, which were in a thick strip shape. However, LB was dominant in Figure 5f, and a mixture of LB and M was also obtained, in which some acicular ferrite (AF) appeared.

The SEM microstructure at $t_{8/5} = 4$ s and $t_{8/5} = 18$ s at $T_{\text{max}} = 1250$ °C is shown in Figure 6. When the cooling rate was fast, many lamellar martensite constituents and

LB appeared in the microstructure, and some AF was distributed among them. M-A constituents were dispersed in the ferrite matrix, with a small content and small granular appearance. When the cooling rate was slightly slow, the M-A constituents appeared in the agglomerated GB, and its content increased significantly, mainly in the form of strips. Meanwhile, lamellar martensite and LB gathered at the adjacent grain boundary.

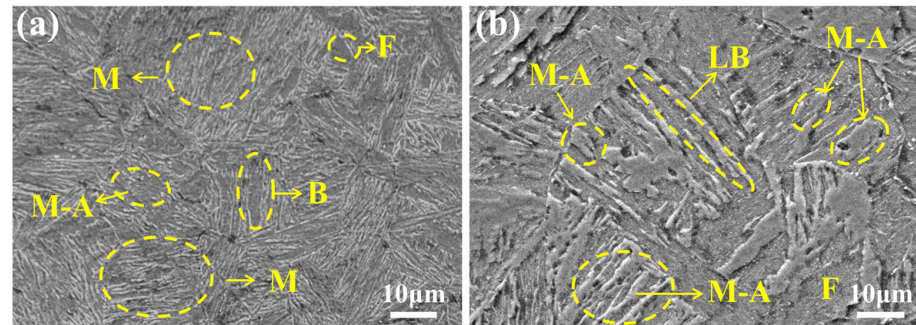


Figure 6. Microstructure (SEM) at (a) $t_{8/5} = 4$ s and (b) $t_{8/5} = 18$ s when $T_{\max} = 1250$ °C.

3.2. Mechanical Properties of the Thermal Simulation Specimen

3.2.1. Micro Vickers Hardness

As shown in Figure 7, the microhardness test results of the CGHAZ obtained by thermal cycle under different $t_{8/5}$ conditions were obtained at different cooling rates when $T_{\max} = 1150$ °C and $T_{\max} = 1250$ °C. Under the premise of the same peak temperature and residence time, the microhardness of the specimen gradually decreased with the decrease of the cooling rate, which meant the microhardness of materials at $t_{8/5}$ from 4 to 6 s decreased faster than that from 6 to 8 s. Accordingly, the grain size also showed an increasing trend (Table 4). The strip-like M-A constituents may cause the hardenability of the microstructure to weaken. As the slowing down of the cooling rate was conducive to the diffusion of carbon elements, the ferrite content increased during the growth of the grain, while the hardness of ferrite was low, and the corresponding microhardness decreased. The microhardness of the microstructure gradually recovered to the hardness of the BM with the further slowing down of the cooling rate. Hence, this also explained the treatment basis that post-weld heat treatment could effectively reduce the hardening of welded joints.

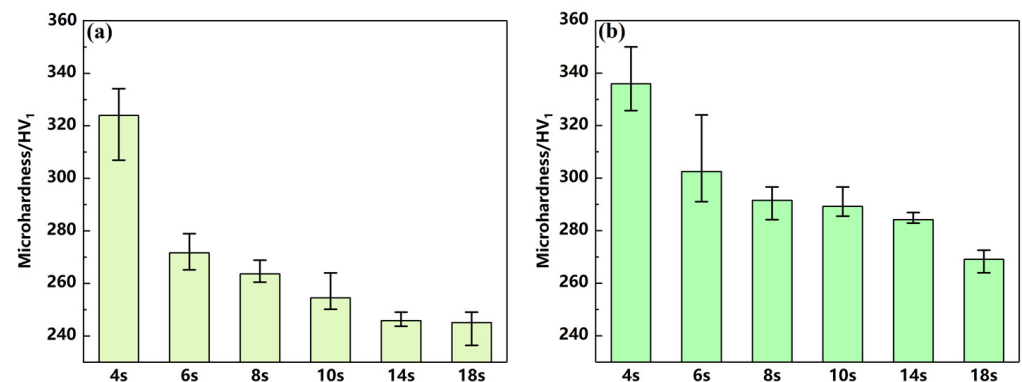


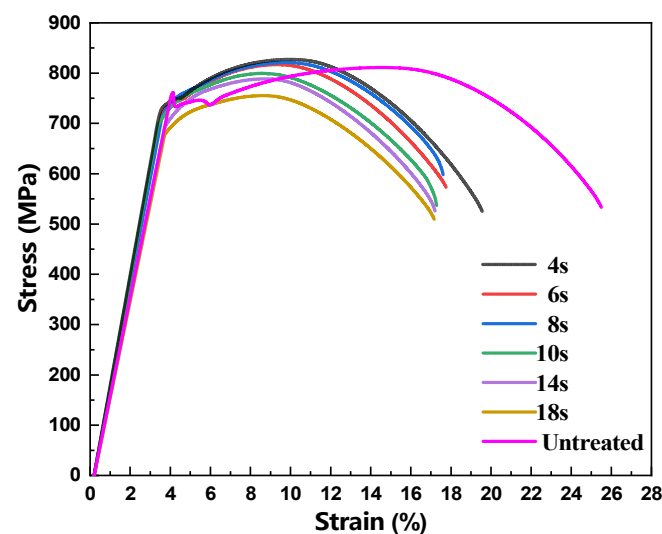
Figure 7. Distribution of microhardness test results for different $t_{8/5}$ values: (a) $T_{\max} = 1150$ °C; (b) $T_{\max} = 1250$ °C.

Table 4. Results of the grain size distribution and hardness at a peak temperature of 1250 °C.

Number	$t_{8/5}$	Range of Grain Size/(μm)	Micro Vickers Hardness/HV ₁
1	4	10.2~20.6	327~350
2	6	18.5~35.2	292~324
3	8	23.8~35.1	284~298
4	10	24.3~35.4	285~297
5	14	28.2~35.8	282~288
6	18	29.3~34.3	264~272

3.2.2. Tensile Property

The strain–stress curves of the thermal simulation specimens with a peak temperature of 1250 °C and different $t_{8/5}$ values are shown in Figure 8, and the effect of the $t_{8/5}$ value on the tensile properties is summarized in Figure 9. As shown in Figures 8 and 9, when $t_{8/5}$ was shorter than 14 s, the yield strength and elongation of the thermal simulation specimen were both lower than those of the BM. When the cooling rate was the highest, namely, $t_{8/5} = 4$ s, the elongation of the specimen was 19.57%. Due to the incomplete austenitizing transformation, many hardened M constituents were generated in the microstructure. When $t_{8/5} = 6$ s, compared with $t_{8/5} = 4$ s, the elongation of the specimen was significantly reduced to 17.87%. As the cooling time increased, the austenitizing process gradually began, and the M-A constituents generated in the microstructure began to increase, so the toughness of the material decreased [21]. The elongation showed a downward trend, which was related to the microstructure change of the material. With the decrease in the cooling rate, although the austenitizing transformation process was sufficient, the ferrite content increased, which was beneficial for the improvement of toughness. With the precipitation of ferrite, the generated LB and M-A constituents enriched many elements near the grain boundary, resulting in the formation of a mixed structure. During the gradual decrease in the grain size, the content of M-A constituents increased, which were mainly distributed near the grain boundary [22], thereby negatively affecting the plasticity of the material and further reducing the elongation. The content of AF and the M-A constituents affected the toughness of the steel [23], but it was obvious that the M-A constituents played a leading role as shown in Figure 8, i.e., that the stress between 6 s and 8 s did not follow the tendency as well as the point ' $t_{8/5} = 8$ s' in Figure 9. To optimize the welding process, when $t_{8/5} = 6$ s, the yield strength of the CGHAZ was 716 MPa, and the tensile strength exceeded that of BM, reaching 817 MPa. Therefore, it is very important to optimize the CGHAZ to obtain high-quality welding joints.

**Figure 8.** Thermal simulation of the micro-zone tensile stress–strain curves when $T_{\text{max}} = 1250$ °C at different $t_{8/5}$ values.

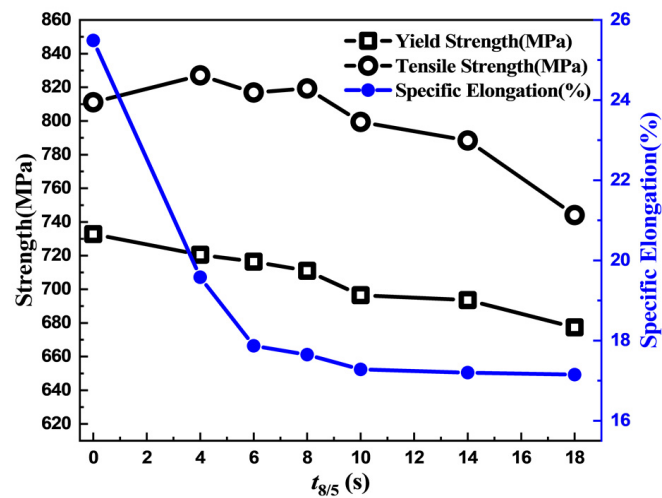


Figure 9. Thermal simulation of the tensile test results when $T_{\max} = 1250$ °C at different $t_{8/5}$ values.

3.2.3. Tensile Fracture

The tensile fracture microstructure of the BM and specimens when $T_{\max} = 1250$ °C under different $t_{8/5}$ values is shown in Figure 10, where all tensile fractures were quasi-cleavage fractures, and there were concave or obvious cracks in the middle of the fracture fiber area. Near the middle crack, there was a brittle fracture, and the ductile fracture was distributed on the fracture with many small dimples, and it was still a ductile fracture in the radial zone. In Figure 10a, the BM was mainly a ductile fracture except for the middle discontinuous area, while there were many 2–3 μm small equiaxial dimples and 7–8 μm large micro-craters along the middle crack edge of the BM in Figure 10b. The small dimples were evenly distributed and had a large depth. The delamination tearing cracks or extrusion middle crack gaps are depicted in Figure 10c–e, whose cooling rates were relatively faster. Compared with the fracture surface of the BM, there was no obvious radiation zone and the fracture mode was mainly brittle, with many secondary small cracks on the fracture surface in Figure 10d. Moreover, a wide crack appeared in the middle of the fracture, and there was an obvious cleavage section near the crack in Figure 10e. The zones A, B, and C represent the crack origin area, radiation area, and fracture area, respectively, and need to be identified and analyzed by different morphologies more clearly. All fractures showed a ductile fracture, and only the middle part had a quasi-cleavage fracture in Figure 10f–h, whose cooling rates were relatively slower. Specifically, there were cleavage section depressions and protrusions in the central fiber area of the fracture, as well as deep strip craters. The number of craters in the radiation zone was reduced, the fracture surface morphology was relatively uniform, and the shear lip area was small, which meant an obvious contraction phenomenon during stretching. Hence, with the decrease in the cooling rate, the tensile fracture of the thermal cycle simulated specimens was more likely to be a ductile fracture.

The SEM microscopic morphology of the dimples near the fracture fiber area is depicted in Figure 11. The dimples near the large craters or cracks showed a tearing shape, with uneven size and morphology, and obvious cleavage sections or faults appeared. There was an obvious lamellar fracture near the large crater on the right part of the boundary in Figure 11a. Moreover, on the left side of the boundary, there were relatively uniform elongated dimples, while on the right side of the boundary, there were brittle fracture characteristics of the flaked concave surface. However, there were obvious cleavage characteristics near the crack in Figure 11b, which were irregular dimples with a small depth far from the crack edge and extending to both sides. Similarly, the morphology around the crack could be found in the expansion path in Figure 11c, with a “step” appearing. Meanwhile, dimples of different shapes were distributed near the strip-shaped craters (Figure 11d), which were generated by the gradual growth of the dimples with small stress

concentrations in the uneven plastic deformation stage of the specimen. The material had a certain plastic reserve, forming many small dimples near the strip crater before fracture. Due to the uneven stress near the dimple of the strip, the shape of small dimples near the dimples of the strip was quite different, while the shape of dimples far from the craters was relatively regular. The small cleavage facet is shown in Figure 11e with elongated but unevenly distributed dimples nearby. Since the dimples in Figure 11f were divided into several morphologies due to the small and medium protrusions of the ductile fracture, one was the uneven dimples mainly with small dimples on the left, the other was the large crater in the middle of the right area with a large depth, and the third was the smooth plane and microcracks on the far right. As the cooling rate decreased, the fracture of the specimen gradually changed into a quasi-cleavage fracture with more obvious toughness.

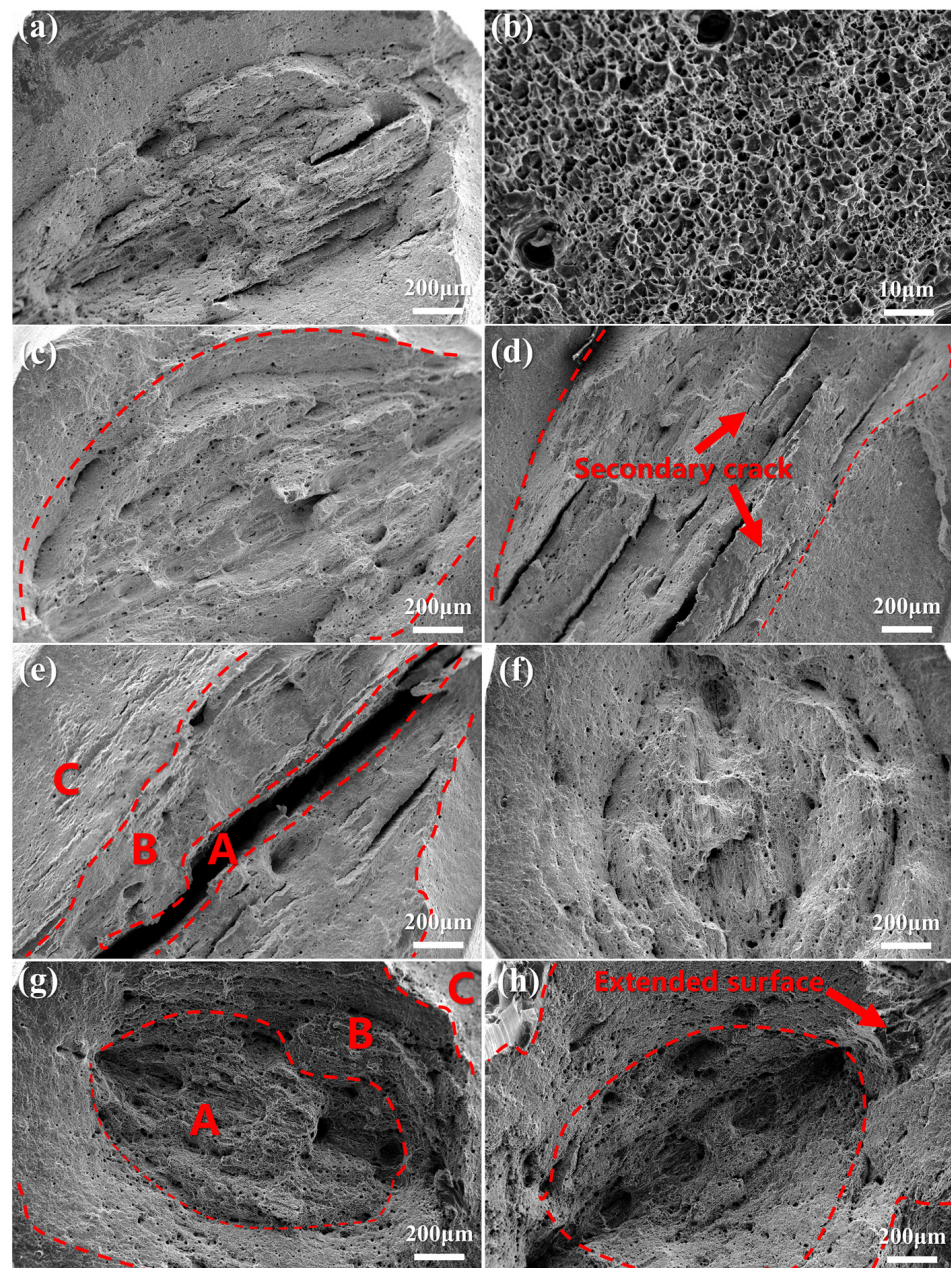


Figure 10. Thermal simulation of tensile fractures at different $t_{8/5}$ values: (a) BM, (b) microporous structure of BM, (c) $t_{8/5} = 4$ s, (d) $t_{8/5} = 6$ s, (e) $t_{8/5} = 8$ s, (f) $t_{8/5} = 10$ s, (g) $t_{8/5} = 14$ s, and (h) $t_{8/5} = 18$ s.

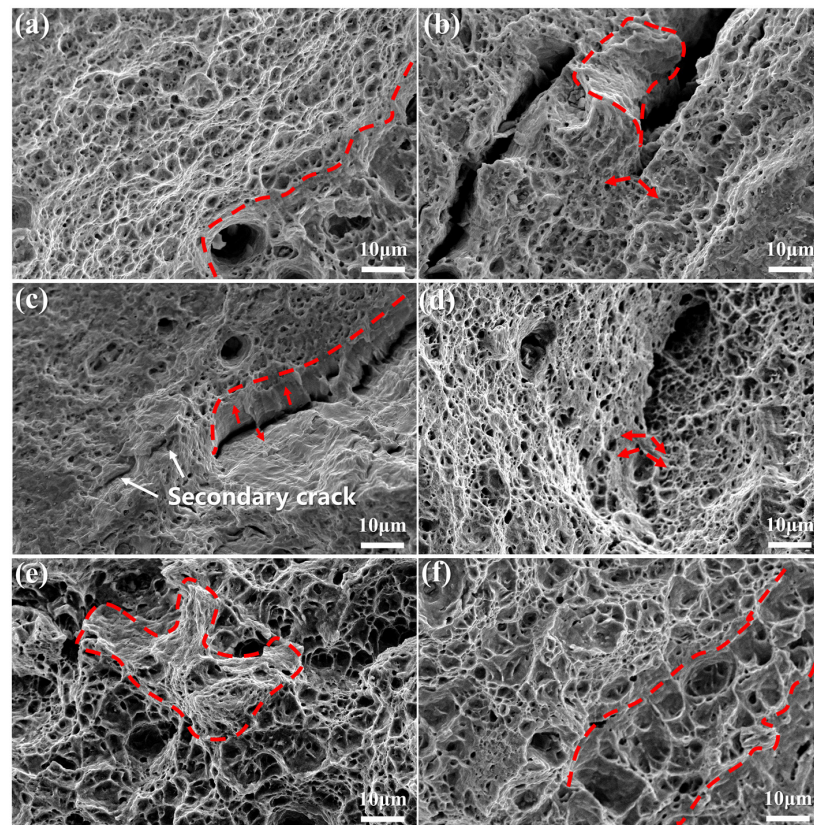


Figure 11. The tensile fiber zone fracture of the thermal simulation specimens at $T_{\max} = 1250\text{ }^{\circ}\text{C}$ under different $t_{8/5}$ values: (a) $t_{8/5} = 4\text{ s}$, (b) $t_{8/5} = 6\text{ s}$, (c) $t_{8/5} = 8\text{ s}$, (d) $t_{8/5} = 10\text{ s}$, (e) $t_{8/5} = 14\text{ s}$, and (f) $t_{8/5} = 18\text{ s}$.

The precipitates and surface morphology of the fracture when $T_{\max} = 1250\text{ }^{\circ}\text{C}$ and $t_{8/5} = 4\text{ s}$ are depicted in Figure 12. Based on SEM and EDS (electronic data sheet analysis, OXFORD instruments, UK), the blocky second phase particles appeared near the microcrack. As shown in Figure 12b, the precipitates were embedded in the cleavage section beside the crack, and a small cleavage facet appeared around them. EDS analysis (Figure 12d) showed that these particles contained trace elements such as Ti, N, C, etc. The addition of trace elements can increase the AF content to a certain extent. Previous studies [21,23] indicated that the increase in the nucleation position of trace elements was conducive to the formation of AF, thus improving the properties of the materials, grain refinement, and the toughness and strength of the materials. The brittle fracture was depicted near the precipitates in Figure 12a, and the morphology of the dimples near the precipitates was not prominent. There were dimples with various depths near the crack, while the cleavage facet appeared at a distance from the crack, where the ductile fracture part of the fracture was a tear dimple with different depths, and small dimples with uneven sizes were distributed near the large dimple (Figure 12c).

Figure 13 shows a further magnification of the ductile fracture characteristics of the fracture. When $t_{8/5} = 6$ and 8 s , many small particles appeared uniformly in the deep dimples. They were attached to the dimple as small particles as shown in Figure 13b,c, and there were no delamination points where plastic flow occurred, indicating that the dimple was generated by the separation of the dispersed secondary phase from the softer matrix. The particles resulting in the dimple could be Mn or Mo primary carbides and carbides contained in the bainite island [24], and EDS confirmed the results, showing Mn and Ti. The dimples of the BM were evenly distributed and had a small depth. When $t_{8/5} = 18\text{ s}$, the dimples were not evenly distributed and had a large depth. No obvious second phase particles were precipitated through observation. Therefore, the cooling speed would affect

the precipitation of the second phase particles, and the cooling rate should be controlled within a reasonable range, such as 6–8 s, to facilitate the precipitation of the second phase particles to play a strengthening role.

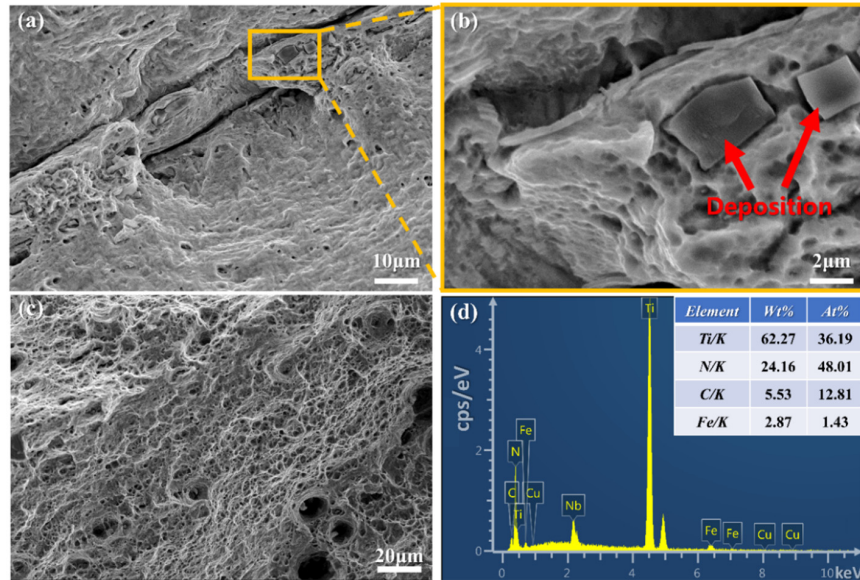


Figure 12. $T_{max} = 1250\text{ }^{\circ}\text{C}$, $t_{8/5} = 4\text{ s}$: (a) precipitates; (b) enlarged view; (c) microstructure; (d) EDS analysis of particles presented in (b).

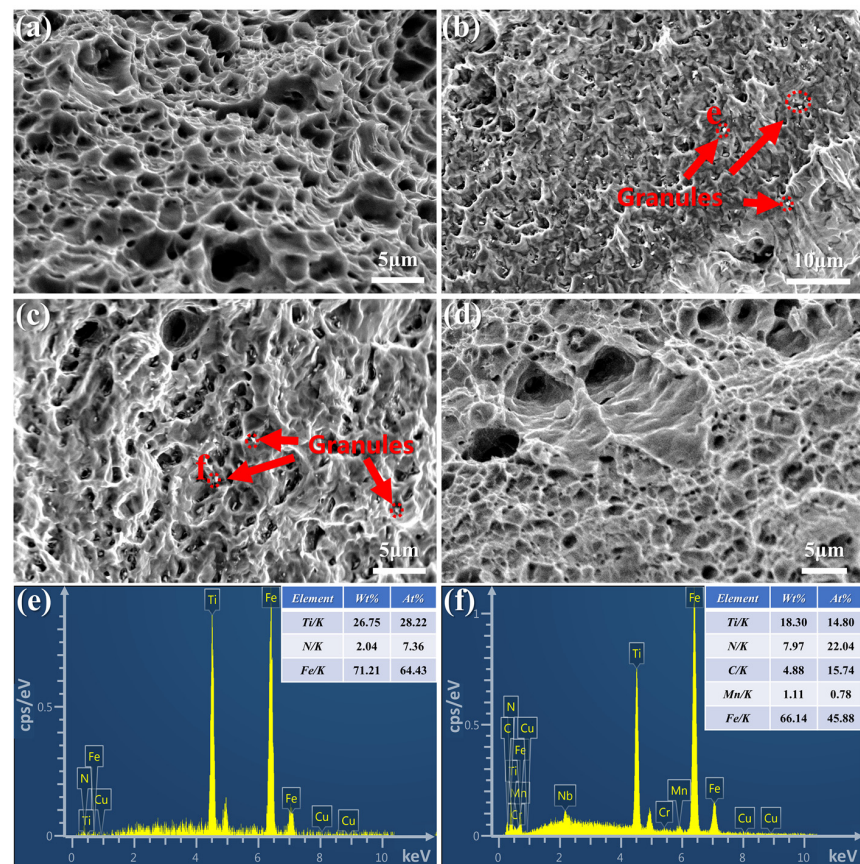


Figure 13. The fracture appearance: (a) BM dimple; (b) $t_{8/5} = 6\text{ s}$ dimple magnification; (c) enlarged image of the $t_{8/5} = 8\text{ s}$ dimple; (d) enlarged view of the $t_{8/5} = 18\text{ s}$ dimple; (e,f) EDS analysis of particles presented in (b) point e and (c) point f, respectively.

4. Discussion

4.1. Analysis of the Phase Transition Mechanism of the Second-Phase Particles

4.1.1. Mechanism Analysis of Microstructure Transformation at Different Cooling Rates

According to the above analysis, the microstructure was rapidly cooled from 800 to 500 °C with a cooling rate of 75 °C/s when $t_{8/5} = 4$ s, which was still supercooled austenite. As the cooling rate of the undercooled austenite slowed down, it was cooled to below 350 °C with a cooling rate of 18.75 °C/s. Accounting for the short time of $t_{8/5}$, the cooling rate exceeded the critical cooling rate of martensite and inhibited the diffusion of carbon atoms. The iron lattice was rearranged in a tangential transformation mode, from FCC γ -Fe to BCC α -Fe, and most of the carbon atoms were retained in α -Fe to form a supersaturated solid solution with LM retained at room temperature [22]. When $t_{8/5}$ was 6–18 s, the cooling time increased between 800 and 500 °C, and the diffusion of carbon could not be completely suppressed. Therefore, part of the undercooled austenite underwent bainite transformation, namely, intermediate temperature transformation. When the temperature dropped to 500 °C, the microstructure was a mixture of supercooled austenite and bainite. As the temperature continued to decrease, the austenite without phase transformation was transformed into LM at the subsequent cooling rate. In the range of 800–500 °C, with the increase in the cooling time, the carbon had sufficient time to diffuse and transform into GB through semi-diffusion phase transformation, and the subcooled austenite that occurred during bainite phase transformation increased. Hence, the LM gradually decreased, and the GB gradually increased with the increase in the cooling time.

4.1.2. Analysis of the Phase Transition Mechanism of the Second-Phase Particles

When $t_{8/5} = 4$ s, there were 2–5 μm square precipitates in the specimen, whose chemical composition was TiCN or TiC, forming a strengthening phase. When $t_{8/5} = 8$ –14 s, the cooling rate decreased, and smaller-sized particles appeared in the tensile fracture, which were distributed inside the fracture dimples and were mainly composed of carbides such as Ti, Mn, and Mo. Ti is an element that can narrow the γ -phase region, and it formed a high melting-point compound with C and N, which could be used as a crystal core and played a role in refining the grains. In addition, the content of N in the material could be reduced in the process of combining with the element of N, where the resulting compound could further promote the nucleation of ferrite in austenite [23,24], accounting for precipitation strengthening. Since the peak temperature of the welding thermal cycle was much lower than the dissolution temperature of the strengthening phase TiC, a solid solution of Ti could occur. However, due to the increase in temperature, the strengthening phase had a certain coarsening phenomenon [25]. During the tensile process, due to the difference between the precipitated phase and the matrix, the separation of the precipitated phase and the matrix further formed micropores, thereby completing the failure process. Obviously, with the decrease in the cooling rate, the tensile strength and toughness of the thermal simulation specimens showed a decreasing trend in the fracture process. The precipitation of the second-phase particles in the specimen played a role in dispersion strengthening, but the improvement of the tensile properties was not obvious due to the coarsening of the precipitation of the second-phase particles, which weakened the strengthening effect.

4.2. Influence of M-A Constituents on the Basic Mechanical Properties

The M-A constituents played a vital role in affecting the ductility and brittleness of the material. They formed upper bainite at 500 °C, and the growth rate was very fast. The C had no time to diffuse, while the island-shaped carbon-rich austenite was surrounded by the ferrite. They became martensite, and another part remained to form retained austenite [7]. When $t_{8/5} = 4$ s, the cooling rate was fast and the diffusion time of carbon atoms was shorter, so the formed fine carbon-rich austenite region was the granular M-A phase, which was characterized indistinctly.

Since the M-A constituents were dispersed on the AF matrix, which was the microstructure of GB, the morphology of the M-A constituents was related to the matrix. Therefore,

with the extension of the cooling time, the diffusion ability of the carbon atoms increased, and the carbon-rich austenite of the body region increased. As the cooling progressed, the region transformed into strip-like M-A constituents arranged in parallel on the ferrite matrix, with similar characteristics to the AF matrix. Moreover, an increasing trend was shown in the content of the M-A constituents on the bainitic ferrite matrix with the increase in $t_{8/5}$, accounting for the fact that the residence time at high temperature increased and the diffusion rate of the C atoms increased. Therefore, the carbon was enriched in more austenite grains, where the number and size of carbon-rich austenite regions increased, so the content and size of the M-A constituents formed by the transformation of this carbon-rich austenite increased.

The content and size of the M-A constituents can affect the strength and toughness of the material [26]. When the cooling rate was fast ($t_{8/5} = 4$ s), the granular M-A constituents were dispersed on the ferrite matrix. Meanwhile, the content of the M-A constituents was relatively low and the size was small. When the tensile test was carried out, the external load made the size induced around this part of the ferrite smaller, so the required critical fracture stress became large, resulting in toughness of the specimens. The content of LM gradually decreased with the continuous increase in $t_{8/5}$, while the content of the M-A constituents gradually increased, whose shape gradually became that of a strip. Therefore, the size of the crack induced under the applied load increased, and the critical fracture stress that was required decreased, presenting a downward trend in the toughness. The M-A constituents with a strip or larger range were more likely to be the weak point of stress concentration than the fine-grained M-A constituents, becoming the place of crack initiation and the low-energy propagation channel [16]. With the decrease in the cooling rate, the content of the M-A constituents increased, and the size of the microcracks induced by the external force increased accordingly, so the critical fracture stress also decreased, and the toughness decreased. In addition, the crack initiation sites also increased with the increase in the content of the M-A constituents, and the microcracks easily expanded and connected, which ultimately reduced the toughness of the material. Therefore, the decrease in the martensite content in the material and the increase in the M-A constituents with the change of shape could lead to the decrease in the toughness of the thermal cycle simulated CGHAZ with the decrease in the cooling rate.

4.3. Analysis of the Tensile Fracture Mechanism

The fracture of both the BM and the thermal cycle specimens had stress orientation, showing the characteristics of tensile delamination [27], where there were cracks or extrusion pits rugged along the middle with the elliptic periphery, and most of the fracture was dimples. The fractures could be roughly summarized as the following two types. As shown in Figure 14a, a quasi-cleavage fracture was characterized by obvious brittleness, and a large and deep layered crack appeared in zone A, the crack origin area. Since the content of the M-A constituents in the specimen was higher than that of ferrite, the brittleness characteristic was obvious. Dimples were observed in zone B, the radiation area, but there were still many secondary cracks and large craters with cleavage steps were around them. Zone C, the fracture area, as the shear lip region, showed toughness characteristics and was the last fracture region. Figure 14b shows the quasi-cleavage fractures with few brittleness characteristics. Most of these types remained in specimens when $t_{8/5}$ exceeded 8 s, and the ferrite content was higher than that of the M-A constituents, showing obvious toughness characteristics. Hence, zone A was prone to many large dimples with some cleavage plane steps nearby, while zones B and C both showed dimples with toughness characteristics, and the dimples in zone B were deep and small with a size of about 1–2 μm .

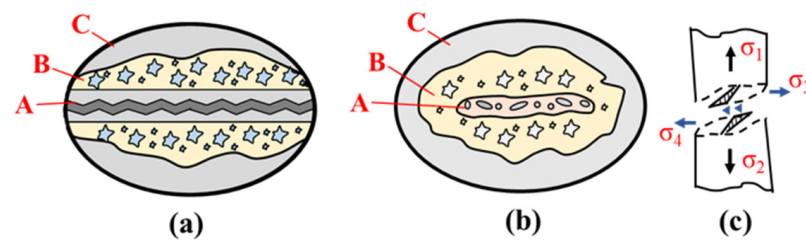


Figure 14. Schematic diagram of the fracture morphology distribution: (a) quasi-cleavage fracture; (b) quasi-cleavage fracture with few brittleness characteristics; (c) schematic diagram of the fracture. (A, B, and C represent the crack origin area, radiation area, and fracture area, respectively, i.e., the three areas of the cross section from inside to outside; σ_1 , σ_2 , σ_3 and σ_4 mean different directions of different stress).

Moreover, under the action of external force, the specimen in Figure 14c was subjected to reverse tensile force in the vertical direction, and the area where the necking occurred would be subjected to triaxial stress [28]. Owing to the stress concentration near the M-A constituents in the region, the bainite elements rotated axially, forming a tensile texture with a specific orientation, and toughening and embrittlement occurred in the tensile direction along the vertical tensile direction. In the center of the specimen, cracking occurred readily around the M-A constituents, which was the origin of the fracture. Under the micropore aggregation mechanism [8], micropores appeared in the crack origin area of the specimen with the action of external forces, and the deformation of the specimen increased, causing the number of micropores to increase gradually. Hence, the middle part of the specimen failed first. At the same time, there were some impurities and oxides in the specimen, which would aggravate the embrittlement degree of the central part. As a result, the specimen weakened the inhibition of the internal microcracks, which were prone to layered fractures along the thickness direction. Due to the large extrusion in the middle, the cross-section of the circular specimen was deformed, and it was roughly elliptical. Then, the micropores accumulated and propagated at an accelerated speed. When the micropores extended to the interface between B and C, the specimen broke instantly and zone C failed until the final rupture.

5. Conclusions

In this study, the influence of the thermal cycle cooling rate of LAHW on the microstructure and properties of the coarse-grain zone of the HAZ in the joint was mainly investigated. The conclusions are as follows:

1. With the increase in $t_{8/5}$, the content of lath martensite decreased, the lath bainite gradually increased and then changed to granular bainite, and the ferrite increased near the M-A constituents. When $t_{8/5}$ increased from 4 to 8 s, the M-A constituents changed from a scattered to a strip shape, and the grain size increased from about 10–20 μm ($t_{8/5} = 4$ s) to about 20–35 μm ($t_{8/5} = 8$ s).
2. When $t_{8/5}$ increased from 4 to 18 s, the microstructure hardness of the thermal simulation specimens decreased from 335 to 275 HV_1 , which was equivalent to the BM. The tensile strength and elongation decreased by 8.8% and 12.5%, respectively. As the content of the M-A constituents increased and the shape changed, the content of ferrite also increased. The thermal simulation specimen with $t_{8/5}$ of 6–8 s had higher strength and good toughness, which could be considered a potential welding parameter reference.
3. When $t_{8/5}$ increased from 8 to 18 s, the M-A constituents began to change from a scattered to a strip shape, which was unfavorable to ductile fracture and reduced the tensile strength. The fracture of the thermal cycle specimens had mixed fracture characteristics, where the brittleness of the fracture was mainly determined by the M-A constituents, and the toughness was mainly determined by ferrite. During the tensile test, the axial force caused the material to tighten, and the transverse stress

was obvious in the part of the M-A constituents that were prone to microcracks and many defects, resulting in cracks, paths, and multi-component layers in the center.

4. The trace elements in the BM appeared in the second phase during the welding thermal cycle, and some of them were in the dimples of the fracture. The second phase was mainly the carbides and nitride of Ti. These elements had a dispersing strengthening impact on the BM. However, due to the low peak thermal cycle temperature and the failure to reach the melting temperature, the precipitates increased, and the strengthening effect was not obvious in the fracture process.

Author Contributions: Conceptualization, J.C. (Jintao Chen); methodology, X.Z. and J.C. (Jingqing Chen); validation, Z.Z. (Zhenlin Zhang); formal analysis, J.C. (Jintao Chen); investigation, Y.L.; resources, X.Z.; data curation, Z.Z. (Zhiyi Zhang); writing—original draft preparation, J.C. (Jintao Chen); writing—review and editing, J.C. (Jintao Chen) and Z.Z. (Zhenlin Zhang); visualization, Z.Z. (Zhiyi Zhang); supervision, J.C. (Jingqing Chen); project administration, H.C.; funding acquisition, H.C. All authors have read and agreed to the published version of the manuscript.

Funding: This work was funded by the Science and Technology Planning Project of Sichuan Province (No. 2021YFG0085, No. 2022YFG0345).

Institutional Review Board Statement: Not applicable.

Informed Consent Statement: Not applicable.

Data Availability Statement: The raw/processed data required to reproduce these findings cannot be shared at this time as the data also form part of an ongoing study.

Acknowledgments: We would like to thank the Analytical and Testing Center of Southwest Jiaotong University for supporting the analytical measurements.

Conflicts of Interest: The authors declare no conflict of interest.

References

1. Tang, G.; Zhao, X.; Li, R.; Liang, Y.; Jiang, Y.; Chen, H. The effect of arc position on laser-arc hybrid welding of 12-mm-thick high strength bainitic steel. *Opt. Laser Technol.* **2020**, *121*, 105780. [[CrossRef](#)]
2. Xiong, J.; Liu, S.; Zhang, G. Thermal cycle and microstructure of backing weld in double-sided TIG arc horizontal welding of high-strength steel thick plate. *Int. J. Adv. Manuf. Technol.* **2015**, *81*, 1939–1947. [[CrossRef](#)]
3. Layus, P.; Kah, P.; Martikainen, J.; Gezha, V.V.; Bishokov, R.V. Multi-wire SAW of 640 MPa arctic shipbuilding steel plates. *Int. J. Adv. Manuf. Technol.* **2014**, *75*, 771–782. [[CrossRef](#)]
4. Hester, M.W.; Usher, J.M. Recycling welding rod residuals based on development of a top-down nanomanufacturing system employing indexing equal channel angular pressing. *Int. J. Adv. Manuf. Technol.* **2017**, *94*, 1087–1799. [[CrossRef](#)]
5. Wahba, M.; Mizutani, M.; Katayama, S. Single pass hybrid laser-arc welding of 25 mm thick square groove butt joints. *Mater. Des.* **2016**, *97*, 1–6. [[CrossRef](#)]
6. Bunaziv, I.; Akselsen, O.M.; Frostevarg, J.; Kaplan, A.F. Deep penetration fiber laser-arc hybrid welding of thick HSLA steel. *J. Mater. Process. Technol.* **2018**, *256*, 216–228. [[CrossRef](#)]
7. Wang, H.; Yang, L. Effect of different welding energy on microstructure and toughness of HAZ of low carbon bainitic steel. *Int. J. Mod. Phys. B* **2020**, *34*, 2050319. [[CrossRef](#)]
8. Cui, J.; Zhu, W.; Chen, Z.; Chen, L. Microstructural characteristics and impact fracture behaviors of a novel high-strength low-carbon bainitic steel with different reheated coarse-grained heat-affected zones. *Met. Mater. Trans. A* **2020**, *51*, 6258–6268. [[CrossRef](#)]
9. Zhang, K.; Chen, J.Q.; Ma, P.Z.; Zhang, X.H. Effect of welding thermal cycle on microstructural evolution of Al–Zn–Mg–Cu alloy. *Mater. Sci. Eng. A* **2018**, *717*, 85–94. [[CrossRef](#)]
10. Zhao, H.; Palmiere, E.J. Influence of cooling rate on the grain-refining effect of austenite deformation in a HSLA steel. *Mater. Charact.* **2019**, *158*, 109990. [[CrossRef](#)]
11. Zavdoveev, A.; Poznyakov, V.; Baudin, T.; Heaton, M.; Kim, H.S.; Acquier, P.; Skory, M.; Rogante, M.; Denisenko, A. Welding thermal cycle impact on the microstructure and mechanical properties of TMCP steels. *Steel Res. Int.* **2021**, *92*, 2000645. [[CrossRef](#)]
12. Lan, L.; Shao, G. Morphological evolution of HAZ microstructures in low carbon steel during simulated welding thermal cycle. *Micron* **2020**, *131*, 102828. [[CrossRef](#)] [[PubMed](#)]
13. Chen, J.H.; Kikuta, Y.; Araki, T.; Yoneda, M.; Matsuda, Y. Micro-fracture behaviour induced by M-A constituent (Island Martensite) in simulated welding heat affected zone of HT80 high strength low alloyed steel. *Acta Metall.* **1984**, *32*, 1779–1788. [[CrossRef](#)]
14. Wang, X.-N.; Zhao, Y.-J.; Guo, P.-F.; Qi, X.-N.; Di, H.-S.; Zhang, M.; Chen, C.-J. Effect of heat input on M-A constituent and toughness of coarse grain heat-affected zone in an X100 pipeline steel. *J. Mater. Eng. Perform.* **2019**, *28*, 1810–1821. [[CrossRef](#)]

15. Guo, A.; Misra, R.D.; Liu, J.; Chen, L.; He, X.; Jansto, S.J. An analysis of the microstructure of the heat-affected zone of an ultra-low carbon and niobium-bearing acicular ferrite steel using EBSD and its relationship to mechanical properties. *Mater. Sci. Eng. A* **2010**, *527*, 6440–6448. [[CrossRef](#)]
16. Davis, C.L.; King, J.E. Cleavage initiation in the intercritically reheated coarse-grained heat-affected zone: Part I. Fractographic evidence. *Metall. Mater. Trans. A* **1994**, *25*, 563–573. [[CrossRef](#)]
17. Di, X.; An, X.; Cheng, F.; Wang, D.; Guo, X.; Xue, Z. Effect of martensite–austenite constituent on toughness of simulated inter-critically reheated coarse-grained heat-affected zone in X70 pipeline steel. *Sci. Technol. Weld. Join.* **2016**, *21*, 366–373. [[CrossRef](#)]
18. Huda, N.; Wang, Y.; Li, L.; Gerlich, A.P. Effect of martensite-austenite (MA) distribution on mechanical properties of inter-critical reheated coarse grain heat affected zone in X80 linepipe steel. *Mater. Sci. Eng. A* **2019**, *765*, 138301. [[CrossRef](#)]
19. GB/T 6394-2017; Determination of Estimating the Average Grain Size of Metal. CISA, Standardization Administration of China: Beijing, China, 2017.
20. Di, X.; Tong, M.; Li, C.; Zhao, C.; Wang, D. Microstructural evolution and its influence on toughness in simulated inter-critical heat affected zone of large thickness bainitic steel. *Mater. Sci. Eng. A* **2018**, *743*, 67–76. [[CrossRef](#)]
21. Deng, W.; Gao, X.; Qin, X.; Gao, X.; Zhao, D.; Du, L. Effect of cooling rate on microstructure of deformed and undeformed x80 pipeline steels. *Acta Met. Sin.* **2010**, *46*, 959–966. [[CrossRef](#)]
22. Xu, K.; Fang, T.; Zhao, L.; Cui, H.; Lu, F. Effect of trace element on microstructure and fracture toughness of weld metal. *Acta Metall. Sin. (Engl. Lett.)* **2020**, *33*, 425–436. [[CrossRef](#)]
23. Han, C.; Li, K.; Liu, X.; Cao, R.; Cai, Z. Effect of Ti content and martensite–austenite constituents on microstructure and mechanical property. *Sci. Technol. Weld. Join.* **2017**, *23*, 410–419. [[CrossRef](#)]
24. Bassini, E.; Sivo, A.; Ugues, D. Assessment of the hardening behavior and tensile properties of a cold-rolled bainitic–ferritic steel. *Materials* **2021**, *14*, 6662. [[CrossRef](#)]
25. Shi, Z.; Wang, R.; Hang, S.; Feng, C.; Wang, Q.; Yang, C. Effect of nitrogen content on the second phase particles in V–Ti microalloyed shipbuilding steel during weld thermal cycling. *Mater. Des.* **2016**, *96*, 241–250. [[CrossRef](#)]
26. Li, X.; Fan, Y.; Ma, X.; Subramanian, S.; Shang, C. Influence of Martensite–Austenite constituents formed at different intercritical temperatures on toughness. *Mater. Des.* **2015**, *67*, 457–463. [[CrossRef](#)]
27. Yan, W.; Sha, W.; Zhu, L.; Wang, W.; Shan, Y.-Y.; Yang, K. Delamination fracture related to tempering in a high-strength low-alloy steel. *Met. Mater. Trans. A* **2009**, *41*, 159–171. [[CrossRef](#)]
28. Testa, G.; Bonora, N.; Ruggiero, A.; Iannitti, G.; Gentile, D. Stress triaxiality effect on cleavage fracture stress. *Theor. Appl. Fract. Mec.* **2020**, *109*, 102689. [[CrossRef](#)]